

## Article

# Ultra-High-Performance Alkali-Activated Concrete: Effect of Waste Crumb Rubber Aggregate Proportions on Tensile and Flexural Properties

Lei Li <sup>1</sup>, Zhongmin Chen <sup>2</sup>, Weixian Che <sup>3</sup>, Cheng Cheng <sup>4</sup>, Yiwu Chen <sup>5</sup>, Dehui Li <sup>6</sup>, Lianghua Liu <sup>7</sup> and Yongchang Guo <sup>7,\*</sup>

- <sup>1</sup> Infrastructure Department of Maoming Power Supply Bureau of Guangdong Power Grid Co., Ltd., Maoming 525000, China; 13580020513@139.com
- <sup>2</sup> Maoming Power Supply Bureau Project Management Center, Guangdong Power Grid Co., Ltd., Maoming 525000, China; 13727802693@139.com
- <sup>3</sup> Power Grid Planning and Research Center, Guangdong Power Grid Co., Ltd., China Southern Power Grid Co., Ltd., Guangzhou 510006, China; 15915791023@139.com
- <sup>4</sup> Maoming Power Supply Bureau Information Center, Guangdong Power Grid Co., Ltd., Maoming 525000, China; chengcheng114044@163.com
- <sup>5</sup> Guangdong Jialin Construction Co., Ltd., Maoming 525000, China; 18006361185@163.com
- <sup>6</sup> Guangdong Shenghong Construction Engineering Co., Ltd., Dongguan 523808, China; lidh@shenghongcorp.com
- <sup>7</sup> School of Civil and Transportation Engineering, Guangdong University of Technology, Guangzhou 510006, China; 13692740118@163.com
- \* Correspondence: guoyc@gdut.edu.cn

**Abstract:** The declining availability of natural sand resources and the significant carbon footprint associated with the extensive use of cement are posing severe limitations on the advancement and application of ultra-high-performance concrete (UHPC). In this study, waste tyre-derived recycled crumb rubber particles (CR) were employed to replace quartz sand, and an alkali-activated cementitious material was used to produce waste tyre-alkali-activated UHPC (T-UHPAC). The influence of different CR replacement ratios (0%, 5%, 20%, 35%, 50%) on the tensile and flexural performance of T-UHPAC was investigated, and a predictive model for the stress–strain response considering the CR replacement ratio was established. An optimization method for improving the tensile and flexural performance of T-UHPAC was proposed. The results indicate that the effect of rough-surfaced CR on the interfacial properties of concrete differs from that of smooth quartz sand. A CR replacement ratio exceeding 35% led to a reduction in both the tensile and flexural strengths of UHPAC, while a replacement ratio at or below 20% resulted in a superior tensile and flexural performance of T-UHPAC. The established predictive model for tensile performance accurately forecasts the stress–strain behaviour of T-UHPAC under varying CR replacement ratios, with the accuracy improving as the CR replacement ratio increases. By utilizing CR to replace quartz sand in proportions not exceeding 20%, the production of low-carbon UHPC with exceptional comprehensive mechanical properties is achievable. Moreover, the development of T-UHPAC through the comprehensive utilization of waste tyres presents a promising and innovative approach for the low-carbon and cost-effective production of UHPC, thereby facilitating the sustainable development of natural resources. This research represents a significant step towards the widespread adoption and application of UHPC and thus holds substantial importance.

**Keywords:** waste crumb rubber; tensile behaviour; tensile constitutive model; flexural behaviour; ultra-high performance

## 1. Introduction

Currently, the widely researched and applied UHPC is typically composed of a large amount of cement as cementitious materials and reinforced with steel fibres. However,



**Citation:** Li, L.; Chen, Z.; Che, W.; Cheng, C.; Chen, Y.; Li, D.; Liu, L.; Guo, Y. Ultra-High-Performance Alkali-Activated Concrete: Effect of Waste Crumb Rubber Aggregate Proportions on Tensile and Flexural Properties. *Buildings* **2024**, *14*, 1088. <https://doi.org/10.3390/buildings14041088>

Academic Editor: Marco Di Ludovico

Received: 8 March 2024

Revised: 7 April 2024

Accepted: 10 April 2024

Published: 13 April 2024



**Copyright:** © 2024 by the authors. Licensee MDPI, Basel, Switzerland. This article is an open access article distributed under the terms and conditions of the Creative Commons Attribution (CC BY) license (<https://creativecommons.org/licenses/by/4.0/>).

these constituent materials have high carbon footprints. For instance, the production of 1 ton of cement generates around 0.87 tons of CO<sub>2</sub> [1–6]. Additionally, the utilization of aggregates in UHPC, such as natural river sand, has resulted in increased mining costs due to the diminishing availability of natural resources. Coupled with the high cost of steel fibres, this considerably escalates the production expenses of UHPC [7–12]. Consequently, the carbon footprint of UHPC is 2.52 times that of ordinary concrete, and the production cost is 8.3 times higher than that of ordinary concrete [1,13,14]. It is crucial to explore methods for reducing the carbon footprint and production costs of UHPC.

The global annual production of waste tyres exceeds 200 million tons, with China generating approximately 120 million tons of waste tyres per year [15–17]. Currently, China's annual waste tyre recycling capacity is around 6.4 million tons, with a recycling rate of only 5%. The excessive use of natural sand in construction and industrial production has already led to its scarcity and rising costs. Processing recycled waste tyres into rubber powders and steel fibres not only reduces carbon emissions associated with raw material extraction and waste tyre disposal but also reduces the weight of concrete and raw material costs by substituting rubber particles for river sand. This enables resource utilization and promotes a circular economy, offering significant environmental and economic benefits.

The substitution of aggregates with recycled rubber particles has the ability to absorb and disperse stress at crack tips, thereby synergistically enhancing the toughness and post-peak strain behavior of the matrix without significant compromise in strength. This improvement can be further enhanced by incorporating other fibres such as waste tyre steel fibres [18–21]. Alsaif and Alharbi [18] found out that incorporating rubber particles and steel fibres could delay the formation and propagation of micro-cracks by reducing stress concentration at the crack tips compared to conventional concrete.

Furthermore, according to Hesami, et al. [22], the replacement of 15% of sand with rubber particles without the inclusion of fibres led to a reduction of 14.29% in tensile strength and a decrease of 17% in flexural strength. Additionally, there was an increase of 26.47% in water absorption. Although higher rubber content could lead a reduction in the mechanical performance of concrete, the negative effects can be mitigated by judiciously adding steel fibres and silica fume, which have a positive influence on its microscopic interface [23–26]. Zahid and Moein [27,28], in their study on the mechanical properties of recycled aggregate concrete containing crumb rubber, found that flexural strength decreased with CR content increases, with a combination of 5% CR and 2% volume of fibres yielding the highest toughness and ductility. Shahjalal, et al. [29] observed that a mixture of 5% CR and fibres enhanced energy absorption capability, when toughness and ductility gradually decreased with increasing CR content. Guo, et al. [30], in their three-point bending test of recycled aggregate ultra-high-performance concrete, showed that fracture energy initially increased but also decreased with the increase in rubber content. The synergistic effect of recycled rubber powder and steel fibres enhanced the ductility and energy absorption capacity of rubberized ultra-high-performance concrete. Additionally, Aslani et al. [31] pointed out that utilizing rubber aggregates to produce self-compacting rubberized concrete reduced workability but enhanced energy absorption and concrete deformation.

When it comes to the impact of cementitious materials on carbon emissions in UHPC, alkali-activated materials (AAM) are an ideal alternative. AAM are three-dimensional inorganic structures obtained by reacting alkaline activators with silica-alumina-rich raw materials [2,32]. The raw materials used for AAM have a low carbon footprint and are widely available, including materials such as kaolin, feldspar, and other silicate-aluminate materials, as well as industrial solid wastes like slag and fly ash [1]. Using AAM as a binder to replace cement in concrete production can reduce the embodied carbon by up to 80% [33]. Alkali-activated concrete (AAC) not only offers the advantage of being low carbon and environmentally friendly but also exhibits excellent mechanical properties [34]. Gao et al. [35] found that alkali-activated slag-fly ash-based concrete exhibits a chain-like C-A-S-H gel as the primary reaction product, regardless of the slag/fly ash ratio or activator modulus, and higher slag/fly ash ratios result in higher strength and lower porosity. Xie

et al. [36] studied alkali-activated recycled aggregate concrete and found that the matrix of the concrete was very dense and strong, with cracks only occurring in the recycled aggregate and interfacial transition zones (ITZs), leading to significant improvements in energy dissipation and toughness. Lao et al. [37] developed slag-fly ash-based UHPC with compressive strength as high as 222 MPa and exhibiting strain-hardening behaviour under tension. The residual crack width after tensile testing was approximately 10–20  $\mu\text{m}$ . Wang, et al. [38] used rubber particle fines to replace fine aggregates in AAC, and found out that incorporating 5% to 20% rubber particles reduced the overall strength of the concrete but effectively improved its energy absorption capacity by 31.5% to 53.3%. However, compared to ordinary concrete, AAC displays increased brittleness, and its brittleness becomes more pronounced as the compressive strength increases [39].

Existing research in related areas mainly concentrates on the study of high-performance concrete using traditional cementitious materials or on the study of alkali-activated concrete using rubber as aggregates. To effectively recycle and reuse waste tyres in engineering applications and promote sustainable and low-carbon development in the construction materials industry, this study aimed to develop an ultra-high-performance concrete utilizing an alkali-activated cementitious matrix and incorporating waste rubber, known as T-UHPAC (Tyre-Derived Ultra-High-Performance Alkali-Activated Concrete). In this study, crumb rubber (CR) was used to replace fine aggregates in UHPC, and waste-tyre steel fibres were used as reinforcing materials to prepare the T-UHPAC. The influence of different replacement ratios (0%, 5%, 20%, 35%, and 50%) of CR on the tensile and flexural properties of T-UHPAC was investigated through static tests. Furthermore, a predictive model for the tensile stress–strain relationship of T-UHPAC considering the influence of CR replacement ratio on concrete damage was established. The article aimed to present a reliable method for designing environmentally friendly, low-carbon, and performance-stable UHPC, and provide a theoretical and data basis for the advancement and promotion of ultra-high-performance concrete. Figure 1 illustrates the flowchart of this research.

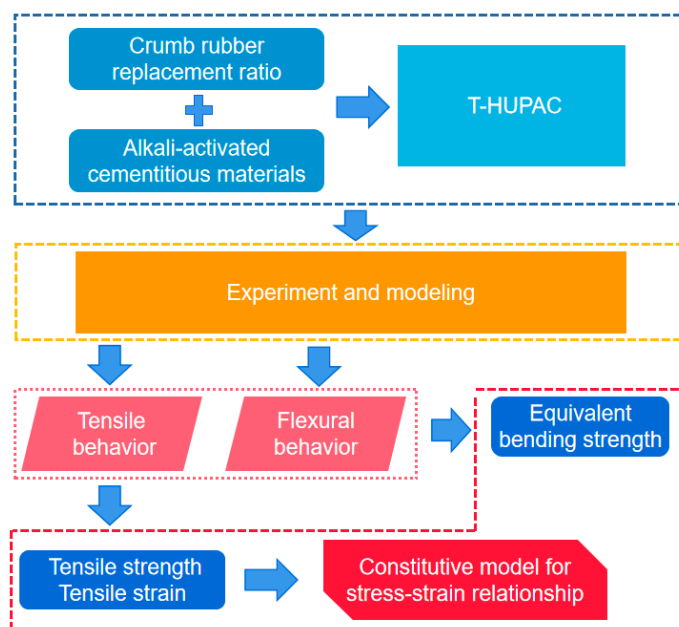


Figure 1. Flowchart.

## 2. Experimental Program

### 2.1. Materials

The composition materials employed in this study for T-UHPAC include a binder mixture consisting of ground granulated blast furnace slag (GGBS, S105 grade), fly ash (FA, Class F), and silica fume (SF, Grade 92). A chemical activator is formed by a sodium hydroxide solution (14 mol/L) and a sodium silicate solution (with a modulus of 2.25).

The aggregate system comprises two different sizes of quartz sand (medium sand, MS, with a particle size range of 200–750  $\mu\text{m}$ , and fine sand, FS, with a particle size range of 45–200  $\mu\text{m}$ ), as well as crumb rubber particles (CR) with  $D_{50} = 450 \mu\text{m}$  recycled from discarded tyres. The quartz sand and rubber powder share similar particle sizes, with densities of  $2.65 \text{ g/cm}^3$  and  $1.13 \text{ g/cm}^3$ , respectively. Recycled steel fibres from discarded tyres (RSF) are used as additional reinforcement.  $\text{BaCl}_2$  is added as an admixture to provide retarding effects. The recycled tyre products CR and RSF are produced by Chengdu Sitong Rubber and Plastic Co., Ltd., Chengdu, Sichuan, China. Please refer to Figures 2–4 and Tables 1 and 2 for specific material parameters.

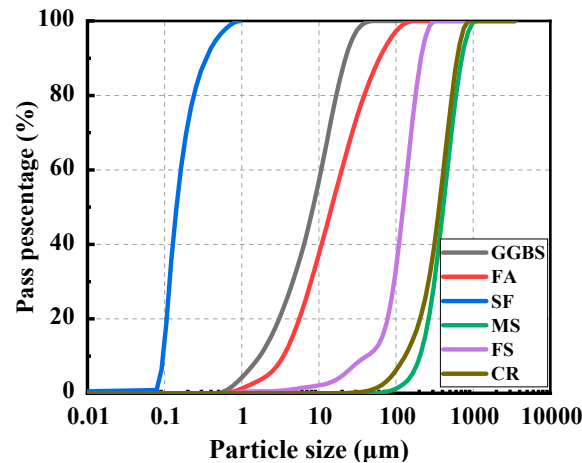
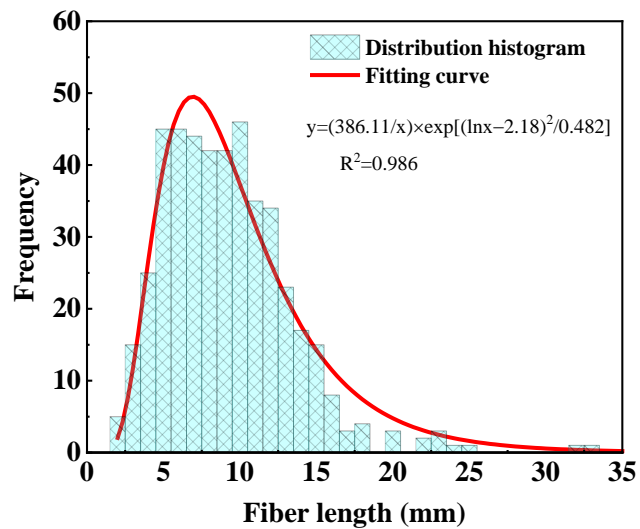


Figure 2. Particle size distribution of cementitious materials and aggregates.



(a) Fibre morphology



(b) Length distribution

Figure 3. Fibre morphology and length distribution of RSF.

The mix proportions and corresponding compressive strengths employed in this study are presented in Table 3. The different experimental groups are named based on the replacement rate of rubber particles. CR was substituted for quartz sand at volumetric replacement ratios of 0%, 5%, 20%, 35%, and 50%. The water-to-binder ratio ( $w/b$ ), which represents the total quantity of water from both activator and additional water, was set at 0.32. The activator was formulated by carefully blending a solution of sodium hydroxide with a sodium silicate solution in a controlled manner, in order to adjust the activator modulus (the molar ratio of  $\text{Na}_2\text{O}$  to  $\text{SiO}_2$  in the activator solution) to 1.5. RSF was incorporated at a 2% vol.

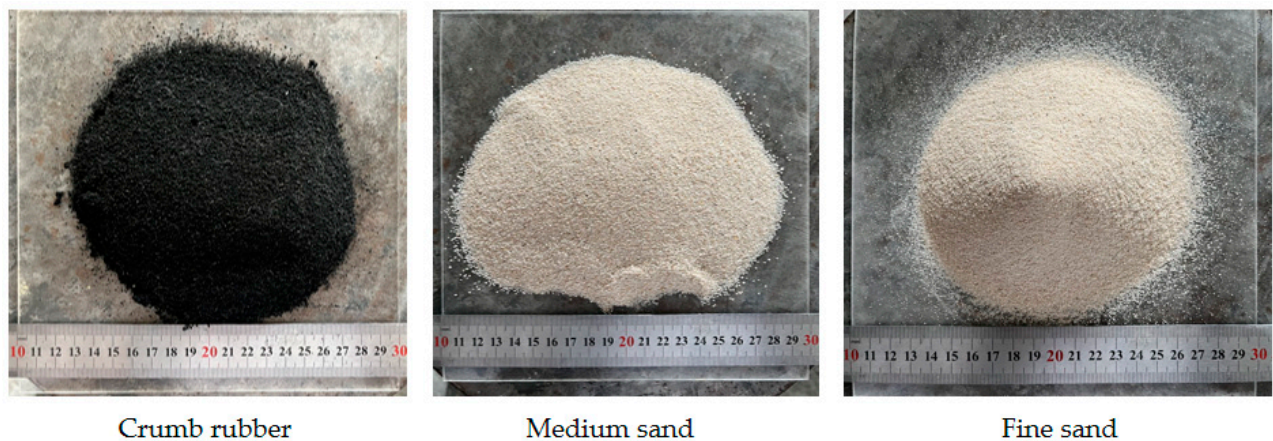


Figure 4. Appearance of aggregates.

Table 1. Chemical composition of cementitious materials.

Oxide	CaO	SiO <sub>2</sub>	Al <sub>2</sub> O <sub>3</sub>	SO <sub>3</sub>	Fe <sub>2</sub> O <sub>3</sub>	MgO	TiO <sub>2</sub>	Other	Loss on Ignition (%)
	wt %								
GGBS	34	34.5	17.7	1.64	1.03	6.01	/	5.12	0.84
FA	4.01	53.97	31.15	2.2	4.16	1.01	1.13	2.37	4.6
SF	/	94.7	/	0.2	/	/	/	5.07	1.5

Note: / denotes the compound is not present in the composition of the material.

Table 2. Properties of RSF.

Fibre Type	Length (mm)	Diameter (mm)	Strength (MPa)	Aspect Ratio (L/d)
RSF	9.92 (Mean value)	0.3	2570	33.07

Table 3. T-UHPAC mix proportions (kg/m<sup>3</sup>).

Mix	GGBS	FA	SF	NaOH	Sodium Silicate Solution	Extra Water	MS	FS	CR	BaCl <sub>2</sub>	RSF	Compressive Strength (MPa)
R-0	688	167	45.0	28.5	307	117	543	362	0.00	9.10	156	148
R-5	688	167	45.0	28.5	307	117	516	344	19.3	9.10	156	137
R-20	688	167	45.0	28.5	307	117	434	290	77.2	9.10	156	105
R-35	688	167	45.0	28.5	307	117	353	235	135	9.10	156	76.6
R-50	688	167	45.0	28.5	307	117	272	181	193	9.10	156	51.3

Note: R-X: X denotes the replacement ratios of CR.

The mixing procedure for the specimens follows the flowchart shown in Figure 5 and can be divided into three main stages. First, the activator was prepared by creating a 14 mol/L sodium hydroxide solution 24 h prior to casting T-UHPAC. After the solution cooled down, it was mixed evenly with the sodium silicate solution and allowed to reach room temperature. Second, the materials were mixed. The fine aggregate was added to a planetary mixer and stirred for 3 min, followed by the addition of the coarse aggregate and another 3 min of mixing until uniformity was achieved. The alkaline activator and additional water were mixed separately and then added to the mixer, followed by an additional 3 min of mixing. The RSF was introduced in the final stage and incorporated into the slurry within 3 min. Lastly, the thoroughly mixed T-AUHPC was poured into dumbbell-shaped moulds for tensile specimens and prism-shaped moulds for flexural specimens. After the initial setting of the specimens, they were covered with plastic film

for curing. After 24 h, the specimens were de-moulded and submerged in a water tank for continuous curing until the age of 28 d.

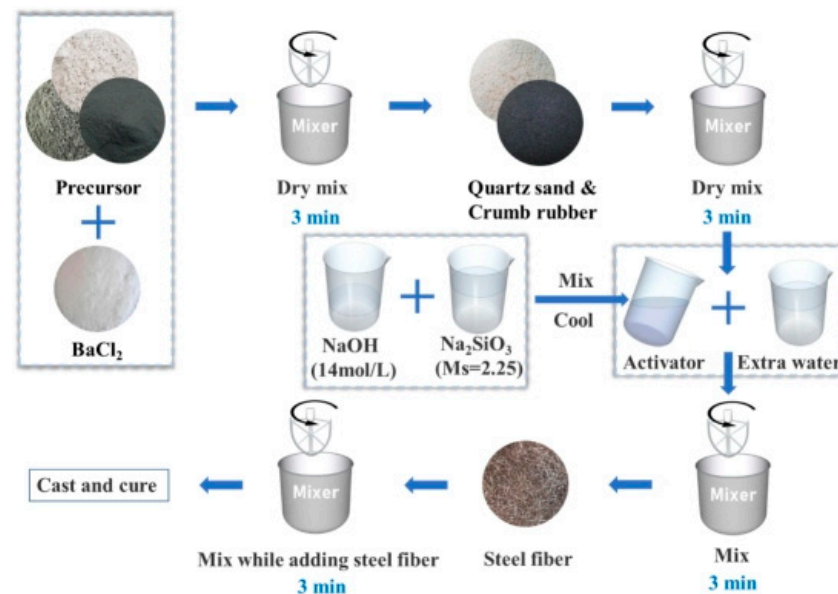


**Figure 5.** Preparation Procedure of T-UHPAC.

## 2.2. Testing Setup

### 2.2.1. Flowability Test

Figure 6 shows the flowability test setup. The flowability test of fresh concrete was conducted according to the code (ASTM-C1437, 2013 [40]). The testing apparatus is shown in the diagram below [2].

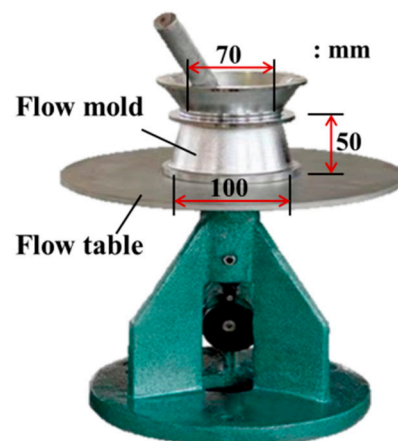


**Figure 6.** Flowability test setup.

### 2.2.2. Axial Tensile Test

Tensile testing was conducted according to the standard T/CBMF 37-2018 [41] (as shown in Figures 7 and 8). Three dumbbell-shaped specimens were prepared for each group to perform axial tensile loading on T-UHPAC, and strain data were recorded using a TDS-540 data logger manufactured by Tokyo Measuring Instruments Laboratory, Tokyo, Japan. The specimens were loaded using displacement control, with a loading rate of 0.06 mm/min. The gauge length of the specimens for measuring strain was set at 100 mm. Prior to the test, strain gauges were attached to the middle region of the gauge length, and two linear variable displacement transducers (LVDTs) were symmetrically placed along the axial direction.

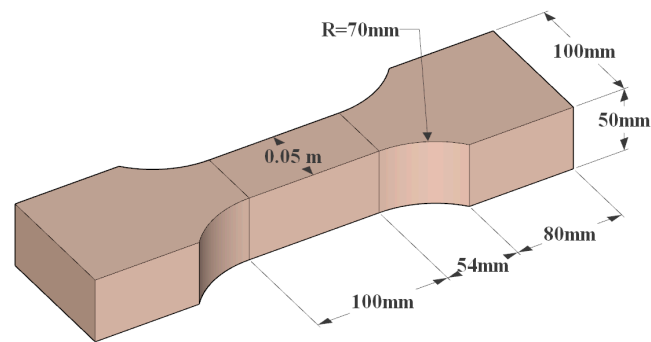


Figure 7. Axial tensile specimen.

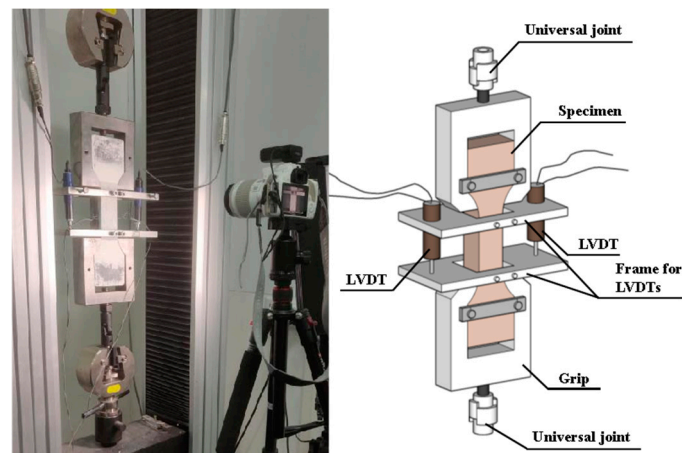


Figure 8. Test set-up and specimen sizes of axial tensile test.

### 2.2.3. Flexural Test

The images captured by the digital image correlation (DIC) system are actually stored in the computer in matrix form. For convenience, we use  $f(x, y)$  to represent the pre-deformation image and  $g(x', y')$  to represent the post-deformation image. The basic principle of the DIC method is shown in Figure 9. First, a reference image subzone is selected in the pre-deformation image, with the measurement point  $(x_0, y_0)$  as the centre and a certain size. Then, through a certain correlation search method, the target image subzone with the maximum correlation to the reference image subzone, centred at  $(x_0', y_0')$ , is found in the post-deformation image. The displacement of the measurement point  $(x_0, y_0)$  is calculated as follows:  $u = x_0' - x_0$ ,  $v = y_0' - y_0$ . The calculated displacement is in pixels. By combining it with calibration results, the actual displacement of the measurement point in the world coordinate system can be obtained.

Flexural testing was conducted following ASTM C1609/C1609M [42], (as shown in Figures 10 and 11). A four-point bending test was performed on the MTS-370 loading system at a displacement rate of 0.075 mm/min. Prior to the test, the side surfaces of the specimens were coated with white paint and marked with black dots to facilitate the measurement of deflection using DIC-3D technology. DIC technology involves capturing high-definition images of the specimen's surface markings using cameras and analyzing the motion of these markings using correlation functions to obtain deformation information [43]. The accuracy of DIC technology has been validated and it can effectively capture key information such as strain and displacement of the specimen [44,45]. Please refer to Figure 8 for the specific testing setup.

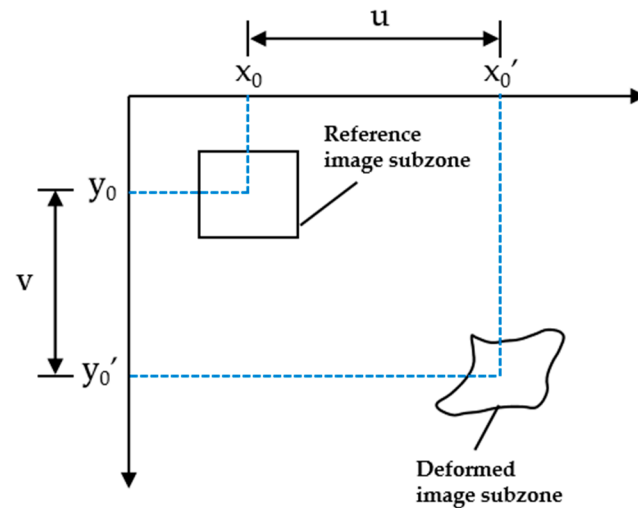


Figure 9. DIC-3D diagram.

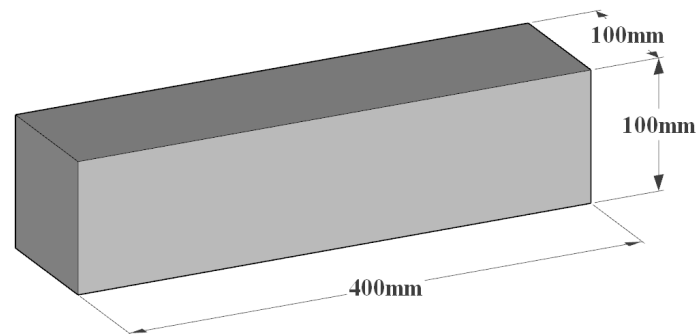


Figure 10. Flexural specimen.

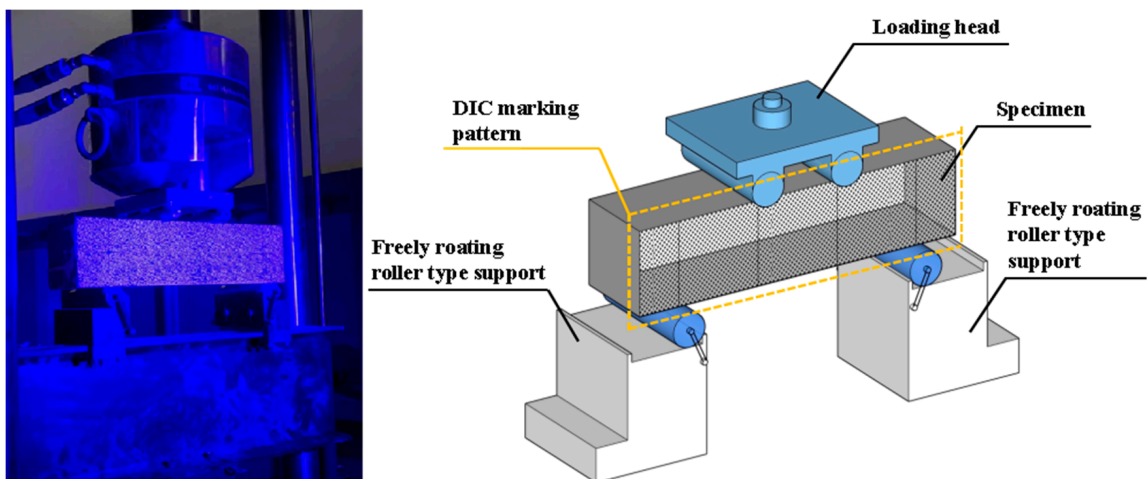


Figure 11. Test set-up and specimen sizes of the flexural test.

#### 2.2.4. SEM and EDS Analysis

The scanning electron microscopy and energy-dispersive X-ray spectroscopy test was conducted using an S-3400N-II scanning electron microscope, produced by Hitachi (Tokyo, Japan). The SEM test mainly characterized the morphology of the interface between the aggregates and the matrix in the fractured cross-sections.

### 3. Results

#### 3.1. Micro Analysis

The microstructural changes in the binder matrix of the slag-fly ash alkali-activated cementitious materials have a significant impact on its macroscopic mechanical properties, and the characteristics of the microstructure mainly depend on the properties of the material [46]. For the R-5 specimens, scanning electron microscopy (SEM) and energy-dispersive X-ray spectroscopy (EDS) were employed to conduct a thorough analysis and examination of the samples. Figure 12 displays the surface morphology of the specimens and the distribution of different elements in the observed areas, with each detected element represented by a different colour.

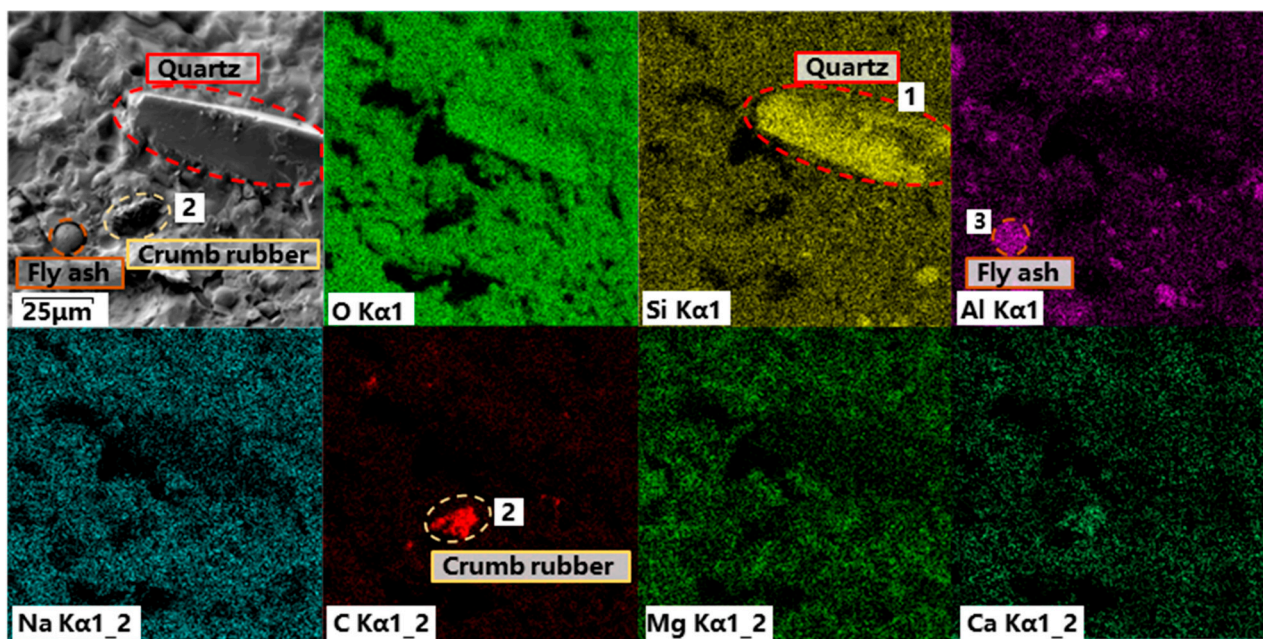


Figure 12. SEM and EDS analysis of R-5.

Upon observation, it is evident that the Si element is significantly enriched in Region 1, and based on the comparison with the surface morphology, it can be inferred that Region 1 corresponds to quartz sand particles. On the other hand, the carbon (C) element is only present in Region 2, which can also be inferred from the surface morphology as corresponding to rubber particles. The aluminium (Al) element is distributed in a point-like manner, including in Region 3, and it can be deduced that Region 3 corresponds to partially hydrated fly ash particles.

Interestingly, no presence of slag was observed in the images, and this could be attributed to the fact that slag exhibits higher reactivity and a higher degree of hydration compared to fly ash. This conclusion can be supported by the uniform distribution of the calcium (Ca) element in the measured area.

From the SEM images showing the morphology of the quartz sand and rubber (Figure 12), it can be observed that the surface of the quartz sand is smooth, while the rubber surface is rough, with numerous protrusions. This explains why the compressive strength decreased as the rubber replacement ratio increased in the fresh T-UHPAC mixture, as it led to the increased number of weak interfaces between the matrix and the aggregates.

On the other hand, it can be observed from Figure 13a that the rubber particles, as a replacement for aggregates, are densely packed within the cementitious materials, which mainly consist of reaction products such as C-S-H, N-A-S-H, and C-A-S-H formed by the active materials of slag, fly ash, and silica fume. However, as highlighted by the yellow line in Figure 13a, due to the poor compatibility of CR, their interface with the cementitious materials is weaker and prone to microcrack development. Consequently, the

rubber particles maintain their relatively intact shape through interface expansion along microcrack paths.

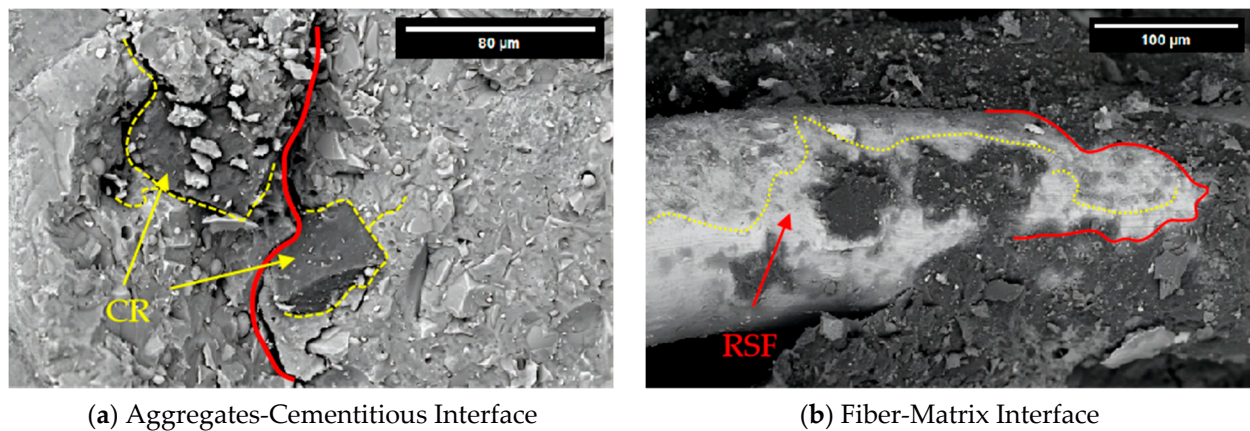


**Figure 13.** SEM analysis of R-5.

Furthermore, the area highlighted by the yellow line in Figure 13b shows the mechanical interlocking and frictional energy between the cementitious materials and the steel fibres, as the fibres are pulled out from the matrix. This interaction provides additional strengthening and energy dissipation mechanisms.

### 3.2. The Effect of Replacement Ratios of Crumb Rubber under Uniaxial Tensile Test

#### 3.2.1. Damage Pattern

Figure 14 shows the damage pattern of the specimens with different CR content in T-UHPAC. The red dashed lines highlight the cracks. During the test, it could be observed that micro-cracks appeared in the middle of the specimen as the tensile loading increased. As the test load further increased, the micro-cracks expanded, accompanied by a slight and noticeable cracking sound. This is consistent with the common tensile failure mode of steel fibre-reinforced UHPAC materials [47,48]. This provides valuable data for subsequent stress-strain analysis of T-UHPAC under uniaxial tensile loading. From the detailed cross-sections, we can see that after the crack initiation, the steel fibres undergo pull-out from the matrix, providing bridging action in the form of fibre pull-out. Moreover, Figure 15 illustrates the flowability of freshly mixed T-UHPAC, as it showed an increase in the replacement ratio of CR, significantly reducing the workability of the fresh paste.

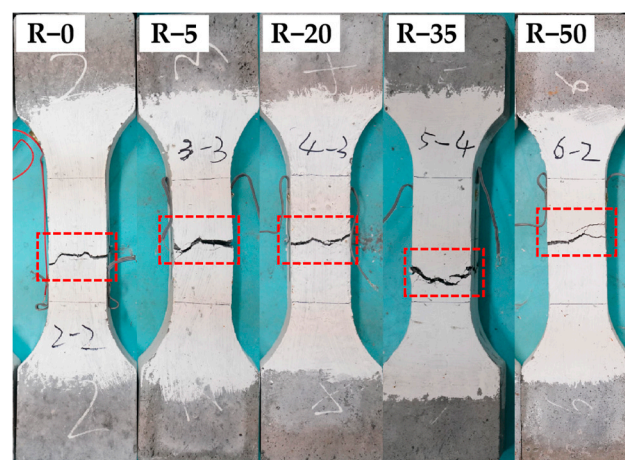


**Figure 14.** Damage pattern.

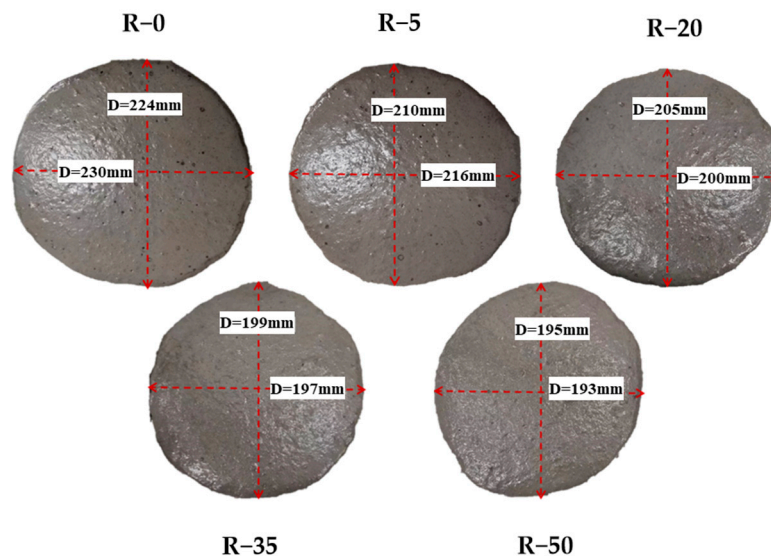


**Figure 15.** Freshly mixed of T-UHPAC.

### 3.2.2. Tensile Stress–Strain Relationship

Notably, it can be seen from Figure 16 that different CR replacement ratios significantly influence the strain-hardening stage of T-UHPAC. The R-0 and R-5 exhibited clear strain-hardening stages, while the test groups with higher CR replacement ratio exhibited very short or even non-existent strain-hardening stages. The CR replacement ratio modified the strain-hardening behavior, which significantly affected the peak tensile strength. The highest tensile strength could be observed in the R-5 within Figure 16. Considering the other test groups, they showed premature termination of the elastic stage, resulting in insufficient strength development, lower initial crack strength, and reduced ductility. The incorporation of CR into the fresh slurry introduced air entrainment, and this was generally attributed to the hydrophobicity of rubber particles and their tendency to repel water [2,49,50]. During vibration, it became challenging to completely remove the entrapped air bubbles. The presence of defects at material interfaces has the potential to diminish bond strength and compromise the bridging strength between the fibres and matrix in T-UHPC. In turn, it could result in a decrease in initial crack strength and hinder the strain-hardening capacity of the material. It is important to note that the incorporation of CR also influences the softening stage curve of T-UHAPC. As evidenced by the data, an increase in the CR replacement ratio tends to flatten the end section of the stress–strain curve.

### 3.2.3. Tensile Strength and Toughness

Figure 17 presents a comprehensive analysis of the correlation between different CR replacement ratios and the resulting changes in the tensile performance, while Table 4 provides precise mechanical performance indicators. It can be observed that the R-5 peak tensile strength is 2.79 MPa, the highest among all groups, surpassing the R-0 by 3.20%. Additionally, the R-20 maintained a peak tensile strength similar to the R-0. The lowest tensile strength is observed in the R-50, measuring 2.16 MPa, which represents a reduction of 22.6% and 25.0% compared to the R-0 and R-5, respectively. In general, no more than 20% CR could lead to an increase in peak tensile strength. This is contrary to some of the existing research findings [31,51]. The reason may be that the hydration behaviour of the slag-fly ash alkali-activated binder material used differs from that of conventional concrete. Additionally, the CR particles used are smaller than 1 mm and have a good particle size distribution with other materials, which allows for an optimization of the internal structure to a certain extent with a CR replacement ratio of less than 20%.

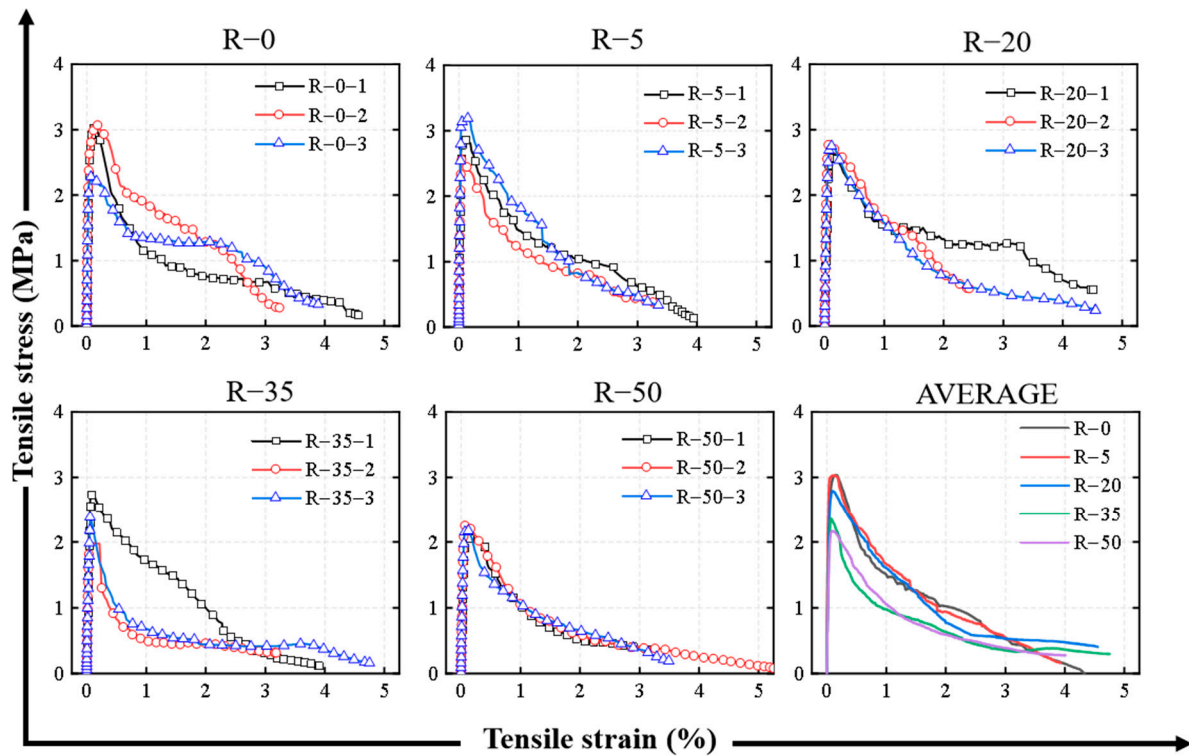


Figure 16. The effect of replacement ratios of crumb rubber on stress–strain curves under tension.

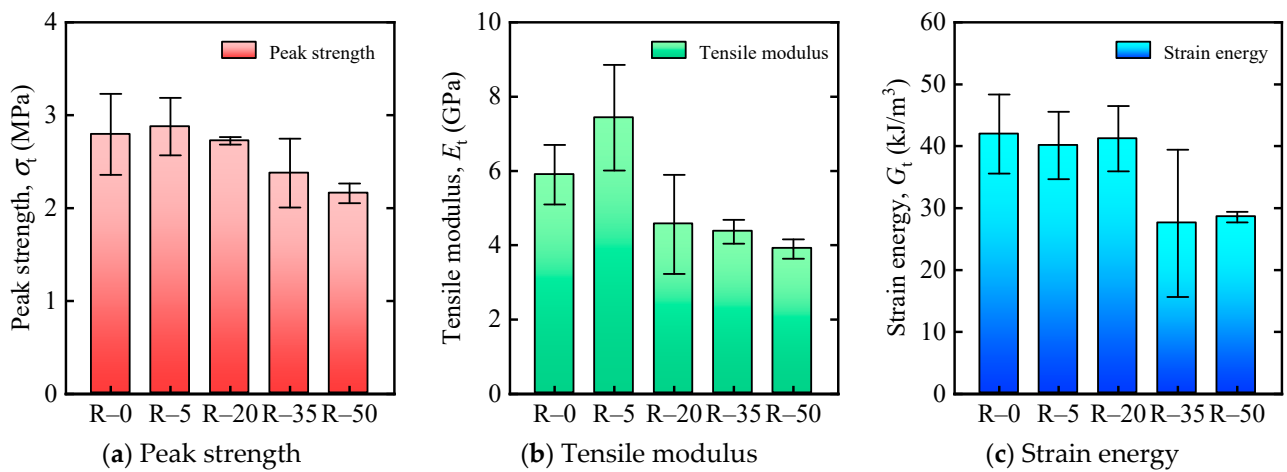


Figure 17. The effect of replacement ratios of crumb rubber on tensile mechanical property index of T-UHPAC. (a) Peak strength; (b) Tensile modulus; and (c) Strain energy.

Table 4. Parameter of axial tensile behaviour.

Mix	Initial Cracking Strength $\sigma_c$ (MPa)	Initial Cracking STRAIN $\epsilon_c$ (%)	Peak Strength $\sigma_t$ (MPa)	Strain Capacity $\epsilon_t$ (%)	Tensile Modulus $E_t$ (GPa)	Strain Energy $G_t$ (kJ/m <sup>3</sup> )
R-0	2.48 (0.29)	0.043 (0.009)	2.79 (0.44)	0.14 (0.06)	5.90 (0.80)	41.40 (7.01)
R-5	2.72 (0.30)	0.037 (0.001)	2.88 (0.31)	0.10 (0.05)	7.43 (1.42)	40.13 (5.43)
R-20	2.55 (0.08)	0.056 (0.015)	2.70 (0.04)	0.11 (0.06)	4.57 (1.33)	41.20 (5.28)
R-35	2.19 (0.46)	0.046 (0.015)	2.38 (0.37)	0.07 (0.03)	4.37 (0.32)	27.53 (11.88)
R-50	2.03 (0.12)	0.052 (0.003)	2.16 (0.11)	0.13 (0.07)	3.90 (0.26)	28.57 (0.85)

Note: the values in parentheses are the standard deviation of test results obtained from three specimens.

The determination of the tensile elastic modulus refers to T/CBMPF 37-2018, and it is obtained from the secant elastic modulus in the elastic stage of T-UHPAC and calculated according to Equation (1). Considering the transient characteristics of strain-hardening in the tensile stress–strain curve of T-UHPAC, the variation of tensile strength could be explored by investigating the influence of the CR replacement ratio on the overall elastic modulus of the material. Figure 17b shows the highest elastic modulus still occurred in R-5, and the trend of elastic modulus with CR replacement ratio is consistent with the compressive strength. This validates that a 5% CR replacement can provide T-UHPAC with a higher elastic modulus, thereby achieving sufficient strength growth in the elastic stage and attaining the highest compressive strength in this study.

The tensile toughness of the material is characterized by the strain energy, which is obtained by integrating the strain along the stress–strain curve to calculate the area under the curve. From Figure 17c, the highest strain energy of 41.40 kJ/m<sup>3</sup> occurred in the R-0, while the R-5 and R-20 are very close, measuring 40.13 kJ/m<sup>3</sup> and 41.20 kJ/m<sup>3</sup>, respectively. It is worth noting that the strain energy of the R-20 and R-35 decreased significantly compared to the other three groups. This could be explained by the increased content of CR weakened the interfacial density of T-UHPAC and affects its bonding performance [2]. Additionally, excessive use of CR led to high plastic viscosity of the fresh mortar and significantly affects fibre dispersion [52,53]. Considering recycled steel fibres with different lengths and thicknesses were used in this study, they are more susceptible to irregular dispersion due to variations in plastic viscosity. It is important to highlight the fact that though the elastic modulus of the R-20 also decreased due to the use of CR, it maintained a comparable strain energy to the R-0 and R-5, due to its similar peak tensile strength and a gradual strength reduction in the softening stage, as compared to the R-5.

$$E_t = \sigma_{c/3} / \varepsilon_{c/3} \quad (1)$$

The stress value at the end of the elastic stage in T-UHPAC is also known as the initial cracking strength. The initial cracking strength can be defined as one-third of initial cracking strength, denoted as  $\sigma_{c/3}$ . The corresponding strain value for  $\sigma_{c/3}$  is denoted as  $\varepsilon_{c/3}$ .

### 3.2.4. Constitutive Model for Stress–Strain Relationship

Drawing from the outcomes of uniaxial tensile stress–strain experiments conducted on T-UHPAC, this study referred to the concrete tensile constitutive model proposed in GB50010-2010 [54]. Modifications were made to the model, taking into consideration the effects of CR on the material damage coefficients (Equations (2)–(5)). The effectiveness of fitting the stress–strain relationship of T-UHPAC was assessed.

$$\sigma = (1 - d_c) E_c \varepsilon \quad (2)$$

$$d_c = \begin{cases} 1 - \rho_t [1.2 - 0.2x^5] & x \leq 1 \\ 1 - \frac{\rho_t}{\alpha_t(x-1)^n + x} & x > 1 \end{cases} \quad (3)$$

$$x = \frac{\varepsilon}{\varepsilon_t} \quad (4)$$

$$\rho_t = \frac{\sigma_t}{E_c \varepsilon_t} \quad (5)$$

The  $d_c$  plays a role in the evolution of damage in concrete under uniaxial tension, while  $\alpha_t$  and  $n$  are the parameter values related to the descending segment of the stress–strain curve under uniaxial tension. The replacement ratio of CR affects the damage evolution of T-UHPAC. A calculation based on Equations (6) and (7) was performed with the fitting effect of the CR replacement ratio and is shown in Figure 18.

$$a_t = r^2 - 0.95r + 0.25, R^2 = 0.86 \quad (6)$$

$$n = 0.91r + 1.92, R^2 = 0.99 \tag{7}$$

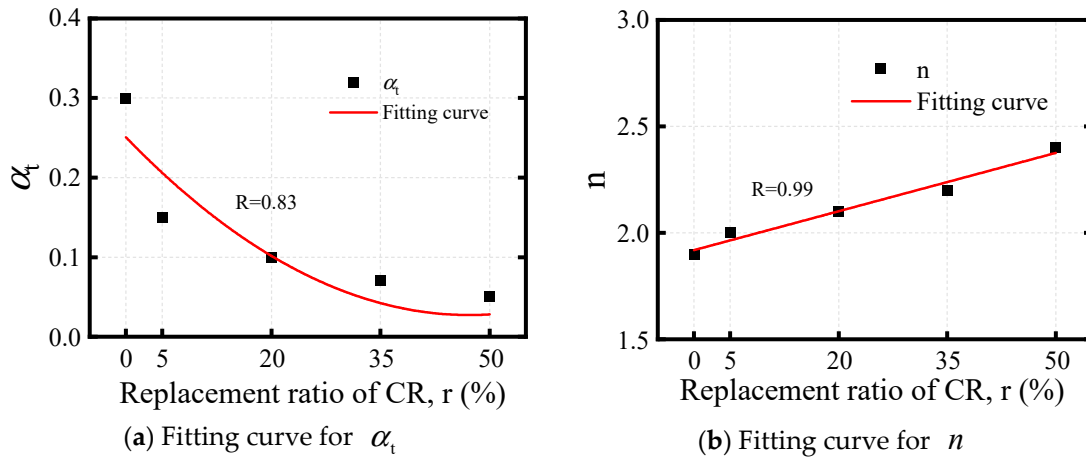


Figure 18.  $\alpha_t$  and  $n$  fitting curve for “r”.

Figure 19 illustrates the stress–strain curves and simulated curves under different CR replacement ratios. At a fixed CR replacement ratio, the modified tensile stress–strain model proposed in this study exhibited a strong correlation with T-UHPAC, as observed. The value fluctuates between 0.87 and 0.98. It is worth noting that  $R^2$  increases with an increase in the CR replacement ratio.

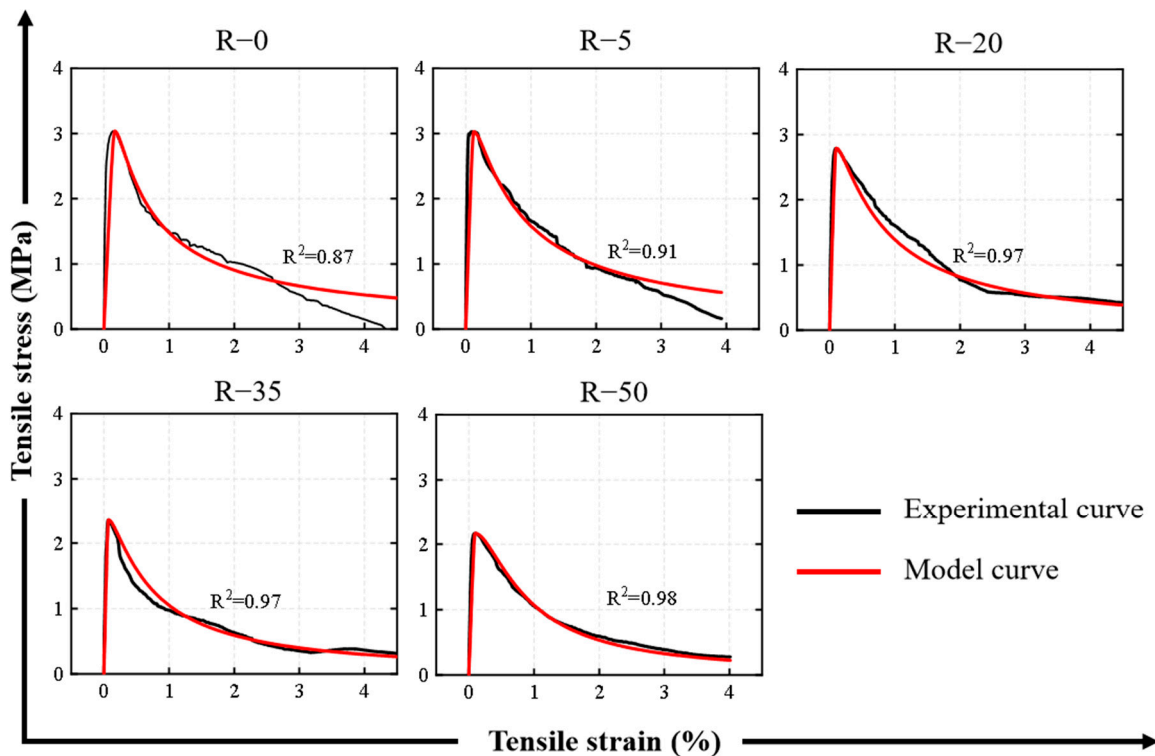


Figure 19. Tensile constitutive model of T-UHPAC.

### 3.3. The Effect of Crumb Rubber Replacement Ratios on Flexural Properties Testing

#### 3.3.1. Failure Mode

Figure 20 shows the surface cracks and section modes of the T-UHPAC beam specimens. Since the crack patterns and section modes of the four test groups with CR additions are almost identical, this study selected R-0 and R-20 for comparison. Figure 20 shows

that the crack patterns in both groups are consistent (as shown in the area marked by the red line), and the crack propagation pattern is nearly consistent with that observed in the tensile test. The section modes were captured using an optical microscope at high magnification, and it can be observed from the figure that there are extracted steel fibres, interface debonding, cracks, and voids in the sections. Comparing Figure 20b,d, there are more and larger voids in the damaged interface of R-20, which confirms that the addition of CR led to more gas in the fresh mortar, forming voids and causing interface defects. After the specimen developed cracks, the steel fibres were slowly pulled out from the matrix, and complete steel fibres can be observed in the sections. Therefore, the steel fibres act as bridges by being pulled out in the flexural properties test, consistent with the tensile test.

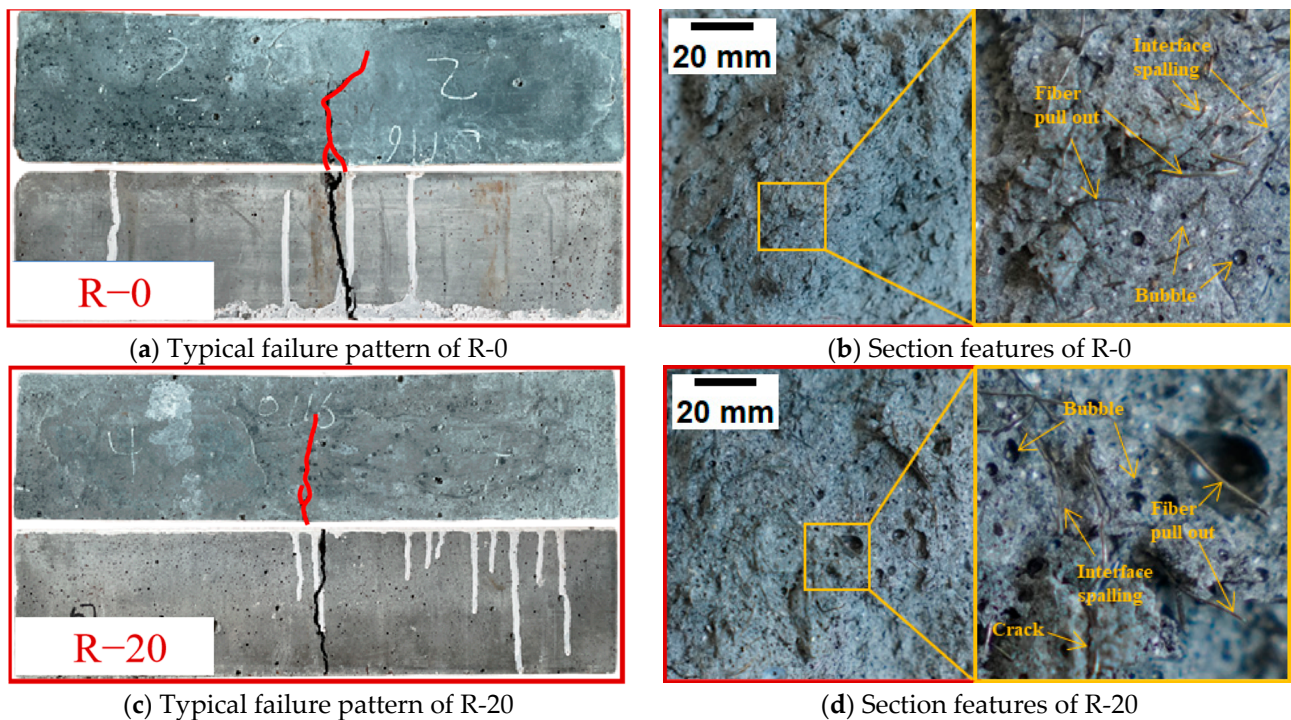


**Figure 20.** Failure mode of flexural test. (a) Typical failure pattern of R-0; (b) Section features of R-0; (c) Typical failure pattern of R-20; and (d) Section features of R-20.

### 3.3.2. Flexural Load–Deflection Relationship

This study employed Digital Image Correlation (DIC) technology to capture deflection changes during the bending tests of the T-UHPAC specimens. The real-time load was collected using the MTS-370 system. The flexural load–deflection curves of T-UHPAC were obtained and presented in Figure 21. Under observation, T-UHPAC exhibited rapid and nearly linear growth in deflection until reaching the peak load. Subsequently, the deflection started to decrease progressively until failure. During the ascending phase of the load, the CR replacement ratio showed minimal influence on the slope of the load–deflection curve, indicating a relatively constant rigidity of the material. However, the peak load was strongly affected by changes in the CR replacement ratio. A higher CR replacement ratio resulted in an early cessation of the load growth phase. In the descending phase of the curve, a higher CR replacement ratio led to a smaller slope, directing to a more gradual deflection decrease.

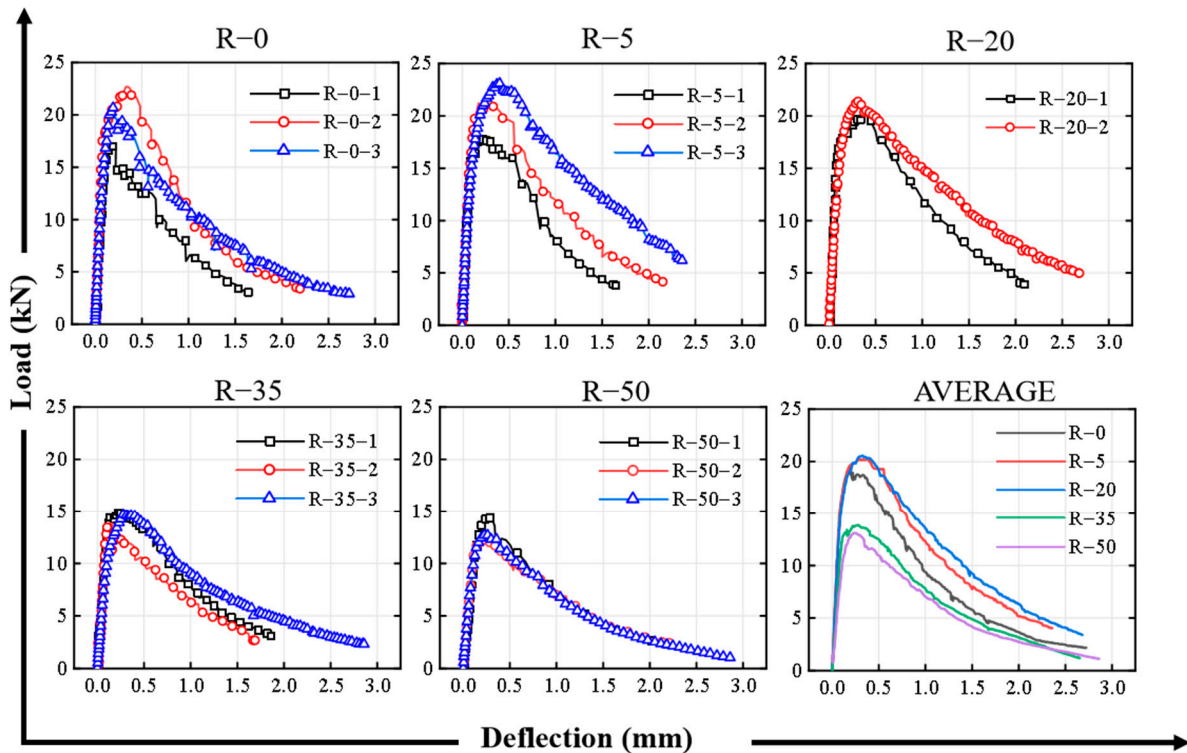


Figure 21. Load–deflection curve of T-UHPAC.

### 3.3.3. Flexural Strength and Toughness

As shown in Figure 22, the basic flexural performance of T-UHPAC is primarily described through the initial cracking load ( $P_c$ ), peak load ( $P_f$ ), corresponding initial cracking deflection ( $\delta_c$ ), peak deflection ( $\delta_f$ ), and flexural strength indices ( $F_c, F_f$ ) as stated in existing research [55] (Figure 17). The flexural strength indices are calculated according to Equation (8).

$$F = \frac{PL}{bd^2} \quad (8)$$

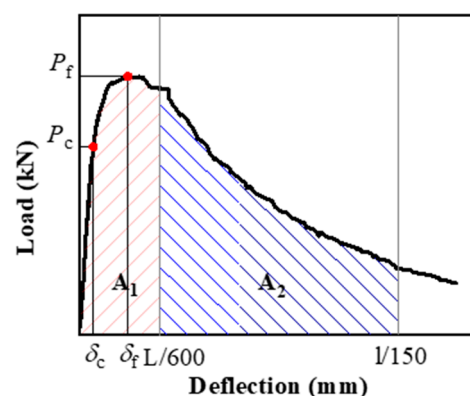


Figure 22. Definitions of the flexural performance parameters.

In Equation (8),  $L$  represents the span of the flexural specimen, while  $b$  and  $d$  refer to the width and height (or thickness) of the specimen's cross-section, respectively.

Table 5 presents the flexural performance indicators obtained from the flexural tests of T-UHPAC. According to the load–deflection curve, there is a noticeable difference between the initial cracking strength and the peak strength, and all specimens exhibited significant strain-hardening behaviour. The R-5 demonstrated the highest initial cracking strength, and

an increase in the CR replacement ratio resulted in a decrease in initial cracking strength, with the maximum reduction of 26.2% observed when the CR replacement ratio increased from 20% to 35%. Except for R-50, the differences in initial cracking deflection among the test groups were not substantial. However, considering  $P_c/\delta_c$ , it is evident that the slope of the ascending phase of the curve decreased with the addition of rubber, which aligns with the findings of a previous study conducted by Xie et al. [40]. The test groups with CR exhibited higher peak deflection compared to R-0, with R-20 showcasing the highest peak deflection of 0.354 mm, representing a 53% increase compared to R-0. The initial cracking strength as well as the peak strength were derived from the R-5 and R-20, with R-5 displaying the highest initial cracking strength and R-20 exhibiting the highest peak strength. This trend is similar to the variation observed in the tensile strength of T-UHPAC. Wanasinghe, Aslani and Dai [24] demonstrated in previous studies that the addition of a certain amount of rubber could enhance the flexural performance of concrete. However, beyond a replacement ratio of 20%, the flexural strength noticeably decreased, causing the load–deflection curve to exhibit a more gradual descent.

**Table 5.** Parameter of flexural behaviour.

Mix	Initial Cracking Load $P_c$ (kN)	Initial Cracking Deflection $\delta_c$ (mm)	$P_c/\delta_c$	Peak Load $P_f$ (kN)	Peak Deflection $\delta_f$ (mm)	$F_c$ (MPa)	$F_f$ (MPa)
R-0	17.5 (2.1)	0.110 (0.033)	166	20.1 (2.9)	0.232 (0.083)	6.99 (0.84)	8.05 (1.15)
R-5	18.8 (1.5)	0.123 (0.059)	171	20.7 (2.7)	0.259 (0.125)	7.35 (0.60)	8.28 (1.07)
R-20	17.6 (1.4)	0.125 (0.049)	150	20.8 (0.8)	0.354 (0.037)	7.02 (0.57)	8.33 (0.33)
R-35	13.0 (1.4)	0.117 (0.011)	112	14.5 (0.6)	0.234 (0.067)	5.18 (0.54)	5.80 (0.23)
R-50	12.0 (1.1)	0.145 (0.021)	81.0	13.2 (1.3)	0.256 (0.034)	4.66 (0.44)	5.29 (0.53)

Note: the values in parentheses are standard deviation of test results obtained from the specimens.

### 3.3.4. Equivalent Bending Strength

Based on ASTM C1609, the equivalent flexural strength and flexural strength ratio at deflections  $L/600$  and  $L/150$  are calculated as toughness indicators to investigate the effect of rubber content on the toughness of T-UHPAC using Equations (8) and (9). In these equations,  $T_n^D$  represents the integral of the load–deflection curve with respect to deflection, which assesses the bending energy absorption capacity of the material.  $f_{e,n}^D$  and  $R_{T,n}^D$  are the equivalent flexural strength and flexural strength ratio corresponding to deflection  $L/n$ , respectively. This study calculated the equivalent flexural strength and flexural strength ratio at deflections  $L/600$  and  $L/150$ .

The results of these calculations are presented in Figure 23 and Table 6. R-5 and R-20 showed higher equivalent flexural strengths compared to R-0 at deflections  $L/600$  and  $L/150$ . However, it should be noted that there was a significant decrease in the equivalent flexural strength when the CR replacement ratio reached 35% or higher. A larger flexural strength ratio indicated greater toughness of the concrete material after cracking. Figure 23 illustrates that the flexural strength ratios at deflections  $L/600$  and  $L/150$  increased with the rubber content, as long as the rubber content remained below 20%. Compared to R-0, R-20 and R-5 demonstrated increases of 11% and 33% in flexural strength ratio, respectively. These findings indicated that the addition of rubber enhanced the flexural toughness of T-UHPAC. However, when the rubber content exceeded 20%, the flexural strength ratios started to decline. The flexural strength ratios of R-35 and R-50 did not show a significant difference from R-0. This suggests that a high rubber content had little influence on the flexural toughness of T-UHPAC. This may be attributed to the fact that excessive replacement of CR led to reduced bond strength within the matrix, resulting in lower initial cracking strength and peak strength. This, in turn, hindered the propagation of cracks.

$$f_{e,n}^D = \frac{n \cdot T_n^D}{bd^2} \quad (9)$$

$$R_{T,n}^D = \frac{f_{e,n}^D}{F_c} \cdot 100\% \quad (10)$$

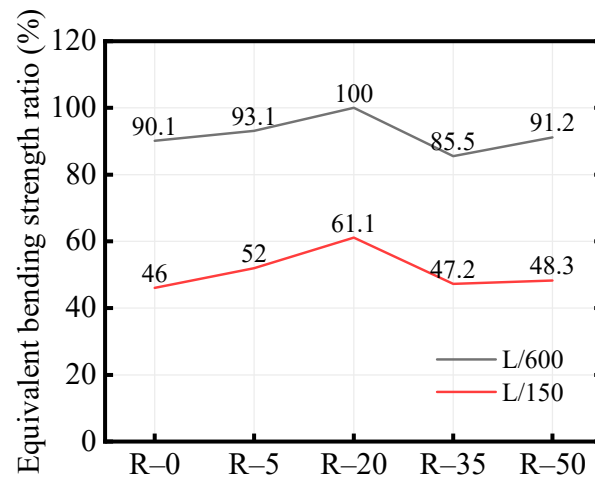


**Figure 23.** The effect of the replacement ratio of CR on the equivalent bending strength ratio.

**Table 6.** Parameter of equivalent bending strength.

Mix	$T_{600}^D$ (J)	$f_{e,600}^D$ (MPa)	$R_{T,600}^D$ (%)	$T_{150}^D$ (J)	$f_{e,150}^D$ (MPa)	$R_{T,150}^D$ (%)
R-0	10.5 (1.6)	6.30	90.1	21.5 (5.7)	3.23	46.0
R-5	11.4 (1.4)	6.84	93.1	25.5 (8.4)	3.83	52.0
R-20	11.7 (0.2)	7.02	100	28.6 (5.9)	4.29	61.1
R-35	7.38 (0.90)	4.43	85.5	16.3 (3.9)	2.45	47.2
R-50	7.08 (0.30)	4.25	91.2	15.0 (0.4)	2.25	48.3

Note: the values in parentheses are standard deviation of test results obtained from the specimens.

#### 4. Conclusions

In this study, T-UHPAC was prepared by using CR as a replacement for quartz sand aggregate and combining a slag-fly ash alkali activation matrix. The microstructure, tensile properties, and four-point bending performance were studied. Based on the existing research findings and the workability characteristics of alkali-activated composite materials used, we did not conduct research on the mechanical properties of T-UHPAC under higher CR replacement ratios. Our focus is primarily on the impact of CR substitution below 50% on alkali-activated ultra-high-performance concrete, and the results are summarized as follows:

- (1) CR did not participate in the formation reaction of C-S-H in the alkali-activated material. It existed in T-UHPAC as a rough-surfaced aggregate. Though it would weaken the interfacial strength between aggregate and matrix because of the significant difference in elastic modulus, the particle size distribution of CR in relation to other materials and the dosage of CR should also be taken into consideration.
- (2) CR caused an air entrainment effect in the fresh mortar of T-UHPAC, generating defects at the material interface and reducing the tensile cracking strength. R-5 showed the highest tensile strength of 2.88 MPa. When the CR replacement ratio was 20% or below, the tensile toughness of T-UHPAC reached its highest value in this study, with only a 3% difference in tensile toughness values between R-0, R-5, and R-20.
- (3) Based on the concrete tensile constitutive model combined with the influence of CR on UHPAC's tensile damage, a predictive model for the stress–strain curve of T-UHPAC considering the CR replacement ratio was proposed. The curve fitting performance improved with increasing CR replacement ratio, showing good predictive accuracy. The development of an effective constitutive model provides valuable support for the research and development of subsequent rubberized concrete performance.

- (4) T-UHPAC exhibited excellent flexural strength and toughness when the CR replacement ratio was not higher than 20%. Among them, R-20 had a flexural strength of 20.8 MPa and the highest equivalent flexural strength ratio, making it the best-performing group in terms of bending performance in this study. Based on the results of tensile tests, bending tests, and compressive strength, this study demonstrates that replacing quartz sand with up to 20% CR is suitable to enhance the tensile and flexural strength, as well as the toughness of T-UHPAC, while maintaining its compressive strength higher than 100 MPa. This provides theoretical support for the design and development of integrated utilization of recycled materials and low-carbon, environmentally friendly, ultra-high-performance building materials.

**Author Contributions:** Conceptualization, L.L. (Lei Li); methodology, L.L. (Lei Li); formal analysis, Z.C.; investigation, L.L. (Lei Li) and Y.G.; resources, C.C. and L.L. (Lianghua Liu); data curation, Z.C. and W.C.; writing—original draft preparation, L.L. (Lei Li); writing—review and editing, L.L. (Lei Li), Y.C. and D.L.; visualization, Y.C. and D.L.; project administration, Y.G.; funding acquisition, Y.G. All authors have read and agreed to the published version of the manuscript.

**Funding:** This research was funded by Maoming Power Supply Bureau, Guangdong Power Grid Co., Ltd., China Southern Power Grid Co., Ltd., grant number 0309002023030201JJ00031.

**Data Availability Statement:** The data presented in this study are available on request from the corresponding author. The data are not publicly available due to confidentiality issues.

**Conflicts of Interest:** Lei Li, Zhongmin Chen, Weixian Che, and Cheng Cheng are employed by the Guangdong Power Grid Co., Ltd., Yiwu Chen is employed by the Guangdong Jialin Construction Co., Ltd., Dehui Liu is employed by the Guangdong Shenghong Construction Engineering Co., Ltd. The remaining authors declare that the research was conducted in the absence of any commercial or financial relationships that could be construed as a potential conflict of interest. The authors declare that this study received funding from the Maoming Power Supply Bureau, Guangdong Power Grid Co., Ltd., the funders had no involvement in the study design, data collection, analysis, interpretation, writing of the article, or decision to submit it for publication. The research was conducted autonomously, ensuring the integrity and objectivity of the findings.

## References

1. Almutairi, A.; Tayeh, B.; Adesina, A.; Isleem, H.; Zeyad, A. Potential applications of geopolymers in construction: A review. *Case Stud. Constr. Mater.* **2021**, *15*, e00733. [[CrossRef](#)]
2. Chen, G.; Zheng, D.-P.; Chen, Y.-W.; Lin, J.-X.; Lao, W.-J.; Guo, Y.-C.; Chen, Z.-B.; Lan, X.-W. Development of high performance geopolymers with waste rubber and recycled steel fiber: A study on compressive behavior, carbon emissions and economical performance. *Constr. Build. Mater.* **2023**, *393*, 131988. [[CrossRef](#)]
3. Pan, H.; Xie, Z.; Chen, G.; Su, J.; Zhuo, K.; Chen, Z.; Lin, J.; Feng, C.; Guo, Y. Dynamic compressive behavior of high-strength engineered geopolymer composites. *J. Build. Eng.* **2023**, *80*, 108036. [[CrossRef](#)]
4. Xiang, L.; Chen, G.; Pan, H.-S.; Wang, Y.-C.; Guo, Y.-C.; Jiang, Z.-X. Analysis of Stress-Strain Behavior in Engineered Geopolymer Composites Reinforced with Hybrid PE-PP Fibers: A Focus on Cracking Characteristics. *Compos. Struct.* **2023**, *323*, 117437. [[CrossRef](#)]
5. Lin, J.-X.; Luo, R.-H.; Su, J.-Y.; Guo, Y.-C.; Chen, W.-S. Coarse synthetic fibers (PP and POM) as a replacement to steel fibers in UHPC: Tensile behavior, environmental and economic assessment. *Constr. Build. Mater.* **2024**, *412*, 134654. [[CrossRef](#)]
6. Miri, M.; Ghasemi, M.R.; Nezhad, H.B. Experimental Investigation of Corrosion Cracking in Reinforced Concrete Beams Containing Nano Wollastonite. *J. Rehabil. Civ. Eng.* **2019**, *7*, 117–138.
7. Arora, A.; Almutairi, A.; Kianmofrad, F.; Mobasher, B.; Neithalath, N. Material design of economical ultra-high performance concrete (UHPC) and evaluation of their properties. *Cem. Concr. Compos.* **2019**, *104*, 103346. [[CrossRef](#)]
8. Dong, Y. Performance assessment and design of ultra-high performance concrete (UHPC) structures incorporating life-cycle cost and environmental impacts. *Constr. Build. Mater.* **2018**, *167*, 414–425. [[CrossRef](#)]
9. He, Z.-H.; Han, X.-D.; Zhang, M.-Y.; Yuan, Q.; Shi, J.-Y.; Zhan, P. A novel development of green UHPC containing waste concrete powder derived from construction and demolition waste. *Powder Technol.* **2021**, *398*, 117075. [[CrossRef](#)]
10. He, Z.-H.; Shen, M.-L.; Shi, J.-Y.; Yalçınkaya, Ç.; Du, S.-G.; Yuan, Q. Recycling coral waste into eco-friendly UHPC: Mechanical strength, microstructure, and environmental benefits. *Sci. Total Environ.* **2022**, *836*, 155424. [[CrossRef](#)]
11. Lin, J.-X.; Su, J.-Y.; Pan, H.-S.; Peng, Y.-Q.; Guo, Y.-C.; Chen, W.-S.; Sun, X.-L.; Yuan, B.-X.; Liu, G.-T.; Lan, X.-W. Dynamic compression behavior of ultra-high performance concrete with hybrid polyoxymethylene fiber and steel fiber. *J. Mater. Res. Technol.* **2022**, *20*, 4473–4486. [[CrossRef](#)]

12. Leila, K.; Kherraf, S.; Hebhoub, H.; Belachia, M. Performance of Concrete Containing Partial Granite and Tiling Wastes as Fine Aggregate. *Civ. Environ. Eng. Rep.* **2023**, *33*, 85–105. [[CrossRef](#)]
13. Shahzad, K.; Zhao, Z. Experimental study of NaOH pretreated crumb rubber as substitute of fine aggregate in concrete. *Constr. Build. Mater.* **2022**, *358*, 129448. [[CrossRef](#)]
14. Sofi, A. Effect of waste tyre rubber on mechanical and durability properties of concrete—A review. *Ain Shams Eng. J.* **2018**, *9*, 2691–2700. [[CrossRef](#)]
15. Li, X.; Li, L.; Zheng, Y.; Li, Y.; Chen, Z.; Xiao, J.; Yuan, M.; Zhang, J.; Pan, Z.; Xiong, Z. A Study of the Compressive Behavior of Recycled Rubber Concrete Reinforced with Hybrid Fibers. *Materials* **2023**, *16*, 4731. [[CrossRef](#)] [[PubMed](#)]
16. Shahjalal, M.; Islam, K.; Batool, F.; Tiznobaik, M.; Ahmed, K.; Alam, M.S.; Ahsan, R. Fiber-reinforced recycled aggregate concrete with crumb rubber: A state-of-the-art review. *Constr. Build. Mater.* **2023**, *404*, 133233. [[CrossRef](#)]
17. Nadi, S.; Beheshti Nezhad, H.; Sadeghi, A. Experimental study on the durability and mechanical properties of concrete with crumb rubber. *J. Build. Pathol. Rehabil.* **2021**, *7*, 17. [[CrossRef](#)]
18. Alsaif, A.; Alharbi, R. Strength, durability and shrinkage behaviours of steel fiber reinforced rubberized concrete. *Constr. Build. Mater.* **2022**, *345*, 128295. [[CrossRef](#)]
19. Assaggaf, R.; Rizwan Ali, M.; Al-Dulaijan, S.; Maslehuddin, M. Properties of concrete with untreated and treated crumb rubber—A review. *J. Mater. Res. Technol.* **2021**, *11*, 1753–1798. [[CrossRef](#)]
20. Wanasinghe, D.; Aslani, F.; Dai, K. Effect of age and waste crumb rubber aggregate proportions on flexural characteristics of self-compacting rubberized concrete. *Struct. Concr.* **2021**, *23*, 2041–2060. [[CrossRef](#)]
21. Chrysanidis, T.; Panoskaltis, V. Experimental investigation on cracking behavior of reinforced concrete tension ties. *Case Stud. Constr. Mater.* **2021**, *16*, e00810. [[CrossRef](#)]
22. Hesami, S.; Hikouei, I.; Emadi, S. Mechanical behavior of self-compacting concrete pavements incorporating recycled tire rubber crumb and reinforced with polypropylene fiber. *J. Clean. Prod.* **2016**, *133*, 228–234. [[CrossRef](#)]
23. Güneysi, E. Properties of rubberized concretes containing silica fume. *Cem. Concr. Res.* **2004**, *34*, 2309–2317. [[CrossRef](#)]
24. Alaloul, W.; Musarat, M.A.; Haruna, S.; Law, K.; Tayeh, B.; Rafiq, W.; Ayub, S. Mechanical Properties of Silica Fume Modified High-Volume Fly Ash Rubberized Self-Compacting Concrete. *Sustainability* **2021**, *13*, 5571. [[CrossRef](#)]
25. Liu, Y.; Shi, C.; Zhang, Z.; Li, N.; Shi, D. Mechanical and fracture properties of ultra-high performance geopolymer concrete: Effects of steel fiber and silica fume. *Cem. Concr. Compos.* **2020**, *112*, 103665. [[CrossRef](#)]
26. Wang, Y.; Chen, J.; Gao, D.; Huang, E. Mechanical Properties of Steel Fibers and Nanosilica Modified Crumb Rubber Concrete. *Adv. Civ. Eng.* **2018**, *2018*, 6715813. [[CrossRef](#)]
27. Hossain, F.M.; Shahjalal, M.; Islam, K.; Tiznobaik, M.; Alam, M.S. Mechanical properties of recycled aggregate concrete containing crumb rubber and polypropylene fiber. *Constr. Build. Mater.* **2019**, *225*, 983–996. [[CrossRef](#)]
28. Khoshroo, M.; Shirzadi Javid, A.A.; Bakhshandeh, N.; Shalchian, M. Investigation of the mechanical properties of concrete containing recycled aggregate and scrap crumb rubber and polypropylene fibers. *Prog. Rubber Plast. Recycl. Technol.* **2020**, *37*, 167–189. [[CrossRef](#)]
29. Shahjalal, M.; Islam, K.; Rahman, J.; Ahmed, K.; Karim, M.; Billah, M. Flexural response of fiber reinforced concrete beams with waste tires rubber and recycled aggregate. *J. Clean. Prod.* **2021**, *278*, 123842. [[CrossRef](#)]
30. Guo, Y.C.; Zhang, J.H.; Chen, G.; Chen, G.M.; Xie, Z.H. Fracture behaviors of a new steel fiber reinforced recycled aggregate concrete with crumb rubber. *Constr. Build. Mater.* **2014**, *53*, 32–39. [[CrossRef](#)]
31. Aslani, F.; Khan, M. Properties of High-Performance Self-Compacting Rubberized Concrete Exposed to High Temperatures. *J. Mater. Civ. Eng.* **2019**, *31*, 04019040. [[CrossRef](#)]
32. De Silva, P.; Sagoe-Crenstil, K.; Sirivivatnanon, V. Kinetics of Geopolymerization: Role of Al<sub>2</sub>O<sub>3</sub> and SiO<sub>2</sub>. *Cem. Concr. Res.* **2007**, *37*, 512–518. [[CrossRef](#)]
33. Van Deventer, J.; Provis, J.; Duxson, P.; Brice, D. Chemical Research and Climate Change as Drivers in the Commercial Adoption of Alkali Activated Materials. *Waste Biomass Valoriz.* **2010**, *1*, 145–155. [[CrossRef](#)]
34. Chen, K.; Wu, D.; Xia, L.; Cai, Q.; Zhang, Z. Geopolymer concrete durability subjected to aggressive environments—A review of influence factors and comparison with ordinary Portland cement. *Constr. Build. Mater.* **2021**, *279*, 122496. [[CrossRef](#)]
35. Gao, X.; Yu, Q.; Brouwers, H.J.H. Assessing the porosity and shrinkage of alkali activated slag-fly ash composites designed applying a packing model. *Constr. Build. Mater.* **2016**, *119*, 175–184. [[CrossRef](#)]
36. Xie, J.H.; Wang, J.; Rao, R.; Wang, C.; Fang, C. Effects of combined usage of GGBS and fly ash on workability and mechanical properties of alkali activated geopolymer concrete with recycled aggregate. *Compos. Part B Eng.* **2018**, *164*, 179–190. [[CrossRef](#)]
37. Lao, J.-C.; Xu, L.-Y.; Huang, B.-T.; Dai, J.-G.; Shah, S.P. Strain-hardening Ultra-High-Performance Geopolymer Concrete (UHPGC): Matrix design and effect of steel fibers. *Compos. Commun.* **2022**, *30*, 101081. [[CrossRef](#)]
38. Wang, H.; Wu, Y.; Cheng, B. Mechanical properties of alkali-activated concrete containing crumb rubber particles. *Case Stud. Constr. Mater.* **2021**, *16*, e00803. [[CrossRef](#)]
39. Ding, Y.; Shi, C.-J. Fracture properties of alkali-activated slag and ordinary Portland cement concrete and mortar. *Constr. Build. Mater.* **2018**, *165*, 310–320. [[CrossRef](#)]
40. ASTM-C1437; Flow of Hydraulic Cement Mortar. ASTM International: West Conshohocken, PA, USA, 2013.
41. T/CBMF 37-2018; Basic Performance and Test Methods of Ultra-High Performance Concrete. China Building Materials Council: Beijing, China, 2018.

42. ASTM C1609-18; Standard Test Method for Flexural Performance of Fiber-Reinforced Concrete (Using Beam with Third-Point Loading). ASTM International: West Conshohocken, PA, USA, 2018.
43. Liu, B.; Guo, J.; Wen, X.; Zhou, J.; Deng, Z. Study on flexural behavior of carbon fibers reinforced coral concrete using digital image correlation. *Constr. Build. Mater.* **2020**, *242*, 117968. [[CrossRef](#)]
44. Liu, F.; Ding, W.; Qiao, Y. Experimental investigation on the flexural behavior of hybrid steel-PVA fiber reinforced concrete containing fly ash and slag powder. *Constr. Build. Mater.* **2019**, *228*, 116706. [[CrossRef](#)]
45. Liu, R.; Li, H.; Jiang, Q.; Meng, X. Experimental investigation on flexural properties of directional steel fiber reinforced rubberized concrete. *Structures* **2020**, *27*, 1660–1669. [[CrossRef](#)]
46. Yang, H.M.; Zhang, S.M.; Wang, L.; Chen, P.; Shao, D.K.; Tang, S.W.; Li, J.Z. High-ferrite Portland cement with slag: Hydration, microstructure, and resistance to sulfate attack at elevated temperature. *Cem. Concr. Compos.* **2022**, *130*, 104560. [[CrossRef](#)]
47. Park, S.H.; Kim, D.J.; Ryu, G.S.; Koh, K.T. Tensile behavior of Ultra High Performance Hybrid Fiber Reinforced Concrete. *Cem. Concr. Compos.* **2012**, *34*, 172–184. [[CrossRef](#)]
48. Sun, T.; Wang, X.; Maimaitiursun, N.; Dong, S.; Li, L.; Han, B. Synergistic effects of steel fibers and steel wires on uniaxial tensile mechanical and self-sensing properties of UHPC. *Constr. Build. Mater.* **2024**, *416*, 134991. [[CrossRef](#)]
49. Tahwia, A.M.; Abd Ellatief, M.; Heneigel, A.M.; Abd Elrahman, M. Characteristics of eco-friendly ultra-high-performance geopolymer concrete incorporating waste materials. *Ceram. Int.* **2022**, *48*, 19662–19674. [[CrossRef](#)]
50. Albidah, A.; Alsaif, A.; Abadel, A.; Abbas, H.; Al-Salloum, Y. Role of recycled vehicle tires quantity and size on the properties of metakaolin-based geopolymer rubberized concrete. *J. Mater. Res. Technol.* **2022**, *18*, 2593–2607. [[CrossRef](#)]
51. Valizadeh, A.; Hamidi, F.; Aslani, F.; Shaikh, F.U.A. The effect of specimen geometry on the compressive and tensile strengths of self-compacting rubberised concrete containing waste rubber granules. *Structures* **2020**, *27*, 1646–1659. [[CrossRef](#)]
52. Lei, D.-Y.; Guo, L.-P.; Li, Y.; Zheng, Z.; Liu, J.-P.; Li, S.-C.; Wang, P.-G.; Li, C.-C.; Mechtcherine, V.; Li, Z.-H.; et al. The investigating on mechanical properties of ultra-high strength and ultra-high ductility cementitious composites (UHS-UHDCC). *J. Build. Eng.* **2021**, *43*, 102486. [[CrossRef](#)]
53. Su, J.-Y.; Chen, G.; Pan, H.-S.; Lin, J.-X.; Zhang, J.; Zhuo, K.-X.; Chen, Z.-B.; Guo, Y.-C. Rubber modified high strength-high ductility concrete: Effect of rubber replacement ratio and fiber length. *Constr. Build. Mater.* **2023**, *404*, 133243. [[CrossRef](#)]
54. GB 50010-2010; Code for Design of Concrete Structures. Ministry of Housing and Urban-Rural Development: Beijing, China, 2010.
55. Li, J.; Chen, J.; Wan, C.; Niu, J. Flexural toughness and evaluation method of steel fiber reinforced self-compacting lightweight aggregate concrete. *Constr. Build. Mater.* **2021**, *277*, 122297. [[CrossRef](#)]

**Disclaimer/Publisher’s Note:** The statements, opinions and data contained in all publications are solely those of the individual author(s) and contributor(s) and not of MDPI and/or the editor(s). MDPI and/or the editor(s) disclaim responsibility for any injury to people or property resulting from any ideas, methods, instructions or products referred to in the content.